Metallophysics and Advanced Technologies
Металлофіз. новітні технол.
Metallofiz. Noveishie Tekhnol.
2026, vol. 48, No. 3, pp. 237–257
https://doi.org/10.15407/mfint.48.03.0237
Reprints available directly from the publisher

PACS numbers: 62.20.M-, 81.40.Jj, 81.40.Np, 81.65.Kn, 82.45.Bb, 82.45.Qr, 92.40.Lg

Stress-Corrosion Cracking of X70 Steel in a Model Low-Acid Soil Environment

L. I. Nyrkova, L. V. Goncharenko, S.O. Osadchuk,
and O. V. Bratochkin

E. O. Paton Electric Welding Institute of N.A.S. of Ukraine,
11 Kazymyr Malevich Str.,
UA-03150 Kyiv, Ukraine

The mechanism of stress-corrosion cracking (SCC) of X70 steel in a weakly acidic model soil environment is investigated using slow strain rate method, voltammetry, optical microscopy, and scanning electron microscopy. New methodological approaches to the study of SCC under thin-film corrosion conditions are developed. The potential ranges, in which SCC mechanism of X70 steel changes, are determined. In the solution, for potentials more positive than –0.816 V (saturated silver-chloride electrode—SSCE), SCC mechanism is anodic dissolution (AD); for negatively than –0.949 V potentials, it is hydrogen embrittlement (HE), and in the range from –0.816 V to –0.949 V, SCC mechanism is mixed (AD+HE). For the model soil environment, a narrowing of the mixed-mechanism region to nearly 0.100 V is established compared to 0.133 V-region for the mixed mechanism in the solution. Moreover, shifting of the lower and upper limits of the mixed-mechanism potentials to more negative values is established, namely, to –1.070 V and –1.170 V, respectively. As determined, the coefficients of susceptibility to SCC, K_S, in the model soil environment are lower than in the solution. At the minimum protective potential of –0.750 V, the differences in the nature of SCC are insignificant; K_S is of 1.30 in the solution and 1.06 in the model soil environment. More consequential changes in SCC of X70 steel under thin-film corrosion influence are observed as the applied potentials are of –0.950 V and

---

Corresponding author: Lyudmyla Ivanivna Nyrkova
E-mail: lnyrkova@gmail.com

Citation: L. I. Nyrkova, L. V. Goncharenko, S. O. Osadchuk, and O. V. Bratochkin, Stress-Corrosion Cracking of X70 Steel in a Model Low-Acid Soil Environment, *Metallofiz. Noveishie Tekhnol.*, **48**, No. 3: 237–257 (2026). DOI: 10.15407/mfint.48.03.0237

–1.050 V. As established, in the solution, SCC at these potentials occurs by hydrogen embrittlement mechanism, which correlates successfully with the brittle nature of specimen fracture and the K_S values of – 2.38 and 2.24. In the model soil environment, SCC occurs by the anodic-dissolution mechanism that is confirmed by ductile characteristics of the failure and K_S values of 1.39 and 1.18.

Key words: pipe steel X70, stress-corrosion cracking, slow strain rate tests, scanning electron microscopy, voltamperometry.

Методою деформації з малою швидкістю, вольтамперометрією, масометрією, сканувальною електронною мікроскопією досліджено механізм корозійного розтріскування криці X70 у слабокислому модельному ґрунтовому середовищі. Розроблено нові методологічні підходи щодо вивчення корозійного розтріскування в умовах тонкоплівкової корозії. Визначено діяпазони потенціялів, в яких змінюється механізм корозійного розтріскування криці X70. У розчині за потенціялів, позитивніших за –0,816 В (відносно насиченого хлоридсрібної електроди порівняння), механізм корозійного розтріскування — локальне анодне розчинення, для потенціялів, від'ємніших за –0,949 В, — водневе окрихчення, від –0,816 до –0,949 В — змішаний механізм. Для модельного ґрунтового середовища встановлено звуження діяпазону змішаного механізму до 0,100 В порівняно із 0,133 В у розчині. Крім того, відзначено зміщення нижньої та верхньої границь діяпазону змішаного механізму до від'ємніших значень — до –1,070 В і –1,170 В відповідно. Визначено, що коефіцієнти схильности до корозійного розтріскування K_S у модельному середовищі нижчі, ніж у розчині. За мінімального захисного потенціялу у –0,750 В відмінності в характері корозійного розтріскування незначні, K_S дорівнює 1,30 у розчині й 1,06 у модельному середовищі. Істотніші зміни в поведінці руйнування криці X70 за впливу тонкоплівкової корозії спостерігалися у разі наведення потенціялів у –0,950 В і –1,050 В. Встановлено, що у розчині корозійне розтріскування за цих потенціялів відбувається за водневим механізмом, що добре корелює з крихким характером руйнування зразка та значеннями K_S у 2,38 і 2,24; у модельному ґрунтовому середовищі корозійне розтріскування перебігає за механізмом анодного розчинення, що підтверджується пластичними характеристиками руйнування зразка та значеннями K_S у 1,39 і 1,18.

Ключові слова: трубна криця X70, корозійне розтріскування, метода деформації з малою швидкістю, сканувальна електронна мікроскопія, вольтамперометрія.

(Received 22 June, 2025; in final version, 27 October, 2025)

1. INTRODUCTION

The reliability of underground gas pipelines is a crucial factor not only for the successful development of Ukraine's economy but also for its security. During operation, underground gas pipelines are subjected to mechanical and corrosive influences, particularly from the soil in cases under disbanded protective coating. Under conditions of cathodic protection beneath a delaminated coating, the initiation and development of stress-corrosion cracking is possible [1, 2].

One of the causes of soil corrosion is the presence of thin water films on metal surfaces [3]. Corrosion of steel in soil is influenced by several factors, including soil moisture, pH, resistivity, concentrations of dissolved salts and oxygen, and concentration and presence of bacteria [4–7].

The corrosion rate of steel in soil can significantly decrease over time due to the formation of oxide layers that limit oxygen diffusion to the surface. However, the corrosion rate increases with rising moisture content up to a critical level. This rate peaks at around 20% moisture content (by mass) for sandy soils, and 25% in clayey, saline, and calcareous soils.

At critical moisture levels, the corrosive activity of soil increases in the following order: calcareous < clayey < saline < sandy [8]. Two types of stress-corrosion cracking (SCC) in pipeline steels have been thoroughly discussed in the literature: those occurring at high pH in concentrated carbonate-bicarbonate solutions (pH $>$ 9.0) [9–11], and in solutions with near-neutral pH (around 6.5) [12–17]. Their mechanisms and patterns have been explored. However, insufficient attention has been paid to SCC in acidic environments.

Notably, studies [18–22] have confirmed the effect of hydrogen-induced plasticity in X70 steel within a certain range of cathodic potentials in acidic solution. This effect reduces the steel susceptibility to SCC by decreasing stress concentration at crack initiation sites and expanding the plastic deformation zone ahead of the crack tip. Nevertheless, the detailed mechanism of hydrogen-induced plasticity and its connection to SCC under cathodic polarization remains unclear and requires further investigation.

According to Ref. [23], in acidic soil, X70 steel is susceptible to SCC during testing with U-bend specimens and notched crack-like specimens. The susceptibility to SCC increased as soil pH decreased. In such acidic soil conditions, there was no correlation between the locations of crack initiation and pitting.

Under alternating wetting/drying cycles, the SCC mechanism for X100 steel at low pH and high dry-to-wet ratios involves both anodic dissolution and hydrogen evolution [24].

In a simulated acidic soil solution, X70 steel shows sensitivity to SCC under cathodic polarization, manifested by loss of ductility and brittle fracture [25]. Lower polarization current accelerates cracking. Stress or strain has a synergistic effect with electrochemical reactions, promoting cathodic hydrogen evolution, thereby making X70 steel more vulnerable to stress corrosion cracking.

In the study [26], using slow strain rate testing, potentiodynamic polarization curve measurement, and surface analysis techniques, it was determined that SCC of X70 steel in acidic soil solution occurs through a mixed mechanism depending on the applied polarization potential. The dominant mechanism changes with different potentials: at less negative potentials, SCC is primarily governed by anodic dissolution; at more negative potentials, hydrogen involvement increases, leading to transgranular cracking. With further negative shifting of the applied potential, SCC becomes fully controlled by a hydrogen embrittlement mechanism, characterized by a river-like brittle fracture surface.

Heat treatment alters the steel microstructure, which in turn affects its susceptibility to SCC. Specifically, steel with a bainitic microstructure exhibits higher susceptibility to SCC in acidic soil, whereas ferritic structures show lower vulnerability.

The influence of inclusions on the initiation of SCC in X70 steel under acidic soil conditions was studied in [27] using slow strain rate testing, scanning electron microscopy, and energy-dispersive x-ray spectroscopy. The results indicated that corrosion cracks do not initiate in X70 steel under anodic polarization. However, cathodic polarization promotes hydrogen evolution, which actively participates in the cracking process. Two types of inclusions have distinct effects on crack initiation: inclusions enriched with Al are brittle and non-coherent with the metallic matrix, leading to easy microcracks' formation at the inclusion–metal interface. In contrast, Si-rich inclusions do not serve as initiation sites for cracks.

In Reference [28], it was found that, under cathodic protection, dissolved oxygen is reduced and the pH in SCC crevice in the initial stage becomes more alkaline. Additionally, the potential within the crevice can reach the protection threshold. The pH difference between the crevice environment and the external surface correlates with the crevice size—the smaller the crevice, the smaller the difference. The presence of CO_2 in the solution inhibits the formation of an alkaline environment. It was also observed that a rust layer sharply reduces the polarization rate in the crevice.

Research on X70 pipeline steel in aqueous peat extract with a pH of 4.5 to 5.5 revealed the formation of an oxide layer composed of four types of iron oxides: lepidocrocite (γ-FeOOH), goethite (α-FeOOH), hematite (α-FeO), and magnetite (FeO). This suggests that the corrosion products on the outer surface of X70 pipelines may form *via* chemisorption and physisorption processes due to interactions between acidic soil particles and the metal surface [29].

The influence of pH on the SCC mechanism of X70 steel in simulated acidic soil solutions was studied using slow strain rate testing, electrochemical polarization curves, electrochemical impedance spectroscopy, and scanning electron microscopy. It was shown that, at pH levels above 5, pH does not significantly affect electrochemical processes during SCC [30]. However, at pH values below 5, hydrogen evolution reactions intensify, increasing cathodic current. Depending on pH and applied potential, the SCC mechanism in X70 steel ranges from anodic dissolution (AD), hydrogen embrittlement (HE), or a combination of both. At –850 mV SCE, SCC occurs *via* HE at pH less than 4, or *via* AD+HE at higher pH.

In study [31], a local supplementary potential model was developed through slow strain rate testing, surface analysis, potentiodynamic polarization, and electrochemical hydrogen permeation methods to illustrate the critical role of strain rate during SCC of X70 steel in acidic soil. According to the model, the density and mobility of local active sites (dislocation initiation points) linearly increase with strain rate. These sites introduce localized negative potentials, affecting electrochemical reactions and thus SCC susceptibility. Maximum SCC susceptibility occurs at a strain rate of 10^{-6} s^{-1} due to enhanced hydrogen evolution from the local supplementary potential effect. When strain rate exceeds 10^{-6} s^{-1}, the dislocation sites move too rapidly for reactive species to couple with them in cathodic reactions, reducing SCC risk. Similarly, the peak hydrogen-permeation current observed at 10^{-6} s^{-1} is also attributed to dislocation density and mobility. Hydrogen diffusion in deformed steel occurs *via* both bulk and dislocation pathways, with the latter becoming dominant as strain rate increases. However, at high strain rates, hydrogen atoms can no longer catch up with rapidly moving dislocations, making bulk diffusion the prevailing mechanism.

The presence of sulphate-reducing bacteria (SRB) may contribute to the susceptibility of X80 steel in acidic soil environments to SCC [32]. In the SRB growth cycle, the polarization resistance first decreases and then increases, being inversely proportional to their number. After 8 days of growth, SRB reach their highest number of 1.42×103 cells/g. Corrosion is highest at this time point, and the SCC mechanism is hydrogen embrittlement. At other stages of SRB growth, the SCC mechanism of X80 steel is anodic dissolution. With the increase of SRB, X80 steel is significantly susceptible to SCC, and the influence of hydrogen is quite obvious.

Studies on the influence of the distribution of the martensite-austenite component in the heat-affected zone of X100 pipeline steel on the mechanism of corrosion cracking in an acidic soil environment showed that the microgalvanic effect, stress/strain concentration, and hydrogen participation contributed to the formation of microvoids at the M–A/matrix interface, which facilitated the initiation and propagation of stress corrosion cracks by their coalescence [33]. SCC microcracks also propagated along the rails of upper bainite, while acicular ferrite and quasi-polygonal ferrite hindered crack propagation.

The study [34] shows that SCC of X70 pipeline steel in acidic soil occurs both in the original microstructure and in the quenched microstructure as the polarization potential decreases. Hydrogen evolution accelerates SCC in both sample types within the potential range of −850 mV to −1200 mV *vs.* SCE. Microstructural strengthening and grain coarsening also increase susceptibility to SCC.

The mechanisms of SCC differ: anodic dissolution is the primary cause when the polarization potential is more positive than the zero current potential, whereas hydrogen embrittlement dominates when the polarization potential is more negative than the zero current potential.

This study is part of a broader research initiative conducted at the E. O. Paton Electric Welding Institute aimed at identifying the specific characteristics of stress corrosion cracking (SCC) in pipeline steels, with particular attention to the effects of thin-film corrosion. The objective of the study is to investigate the patterns of SCC development in X70 steel within a weakly acidic model soil environment under cathodic polarization and to determine potential differences in its progression compared to behaviour in a model soil electrolyte.

The originality of this work lies in the application of novel methodological approaches to studying SCC under thin-film corrosion conditions. This enables the acquisition of new insights into the corrosion cracking behaviour of X70 steel in soil environments. The findings are expected to deepen understanding of SCC mechanisms in main gas pipelines under cathodic protection and offer practical relevance for operating organizations.

2. EXPERIMENTAL/THEORETICAL DETAILS

2.1. Chemical Composition, Microstructure and Mechanical Properties of Steel

The research was conducted on controlled-rolled steel X70. Its chemical composition is given in Table 1. Mechanical properties of steel are

TABLE 1. Chemical composition of steel.

Mn	C	Si	P	S	Nb	Mo	V	Ti	Ni	B
1.71	0.10	0.21	0.01	0.01	0.05	0.03	0.06	0.02	0.03	0.002

TABLE 2. Mechanical properties of X70 steel.

$\sigma_{\text{т}}$, MPa	$\sigma_{\text{в}}$, MPa	δ_5, %
570	485	20

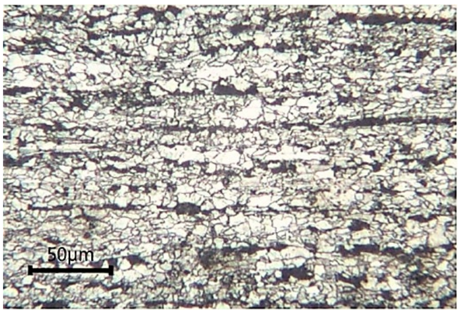

Fig. 1. Microstructure of X70 steel [36].

presented in Table 2 [35].

The microstructure of steel is shown in Fig. 1.

The tests were performed in a solution of 2.28 g/l HCOOH + 54.4 g/l HCOONa + 10.8 g/l KCNS (further, solution), prepared using distilled water and chemical pure reagents, the model soil medium containing 80 g of sand and 20 g of above solution (further, model soil medium).

2.2. Electrochemical Tests

The surface of the specimens was polished on abrasive paper of different grain sizes, degreased with magnesium oxide, washed with distilled water, and dried. Electrochemical measurements were performed according to a three-electrode scheme: the working electrode was a steel specimen, the reference electrode was a silver chloride electrode (SCEE), and the auxiliary electrode was a platinum electrode. Polarization curves were measured on a universal device potentiostat-galvanostat MTech PGP-550F with the software MTech PGP-550F in potentiodynamic mode with a potential sweep rate of 1 mV/s. During the study of the stress-corrosion cracking mechanism, polarization curves were measured at potential scan rates of 0.5 mV/s and 100 mV/s.

2.3. Massometry

Corrosion rate was determined by massometry method. The duration of the tests was 168 hours (1 week). Specimens were weighed on VLR-200 g weight of accuracy class 2, and their area was determined using an electronic calliper. After tests, the corrosion products were removed using an eraser, rinsed with distilled water, dried and weighed. The corrosion rate was calculated from the mass change of specimens and tests duration by the formula:

$$v_{\mathrm{cor}} = \frac{8760 \cdot \Delta m}{S \cdot \tau \cdot \rho}, \tag{1}$$

where δm—mass change of specimens, g; S—specimens area, m^2; τ—tests duration, h; ρ—metal density, g/cm^3; 8760—number of hours per year.

2.4. Slow Strain Rate Tests

A sketch of the test specimen is shown in Fig. 2. The method is based on the deformation of specimen at a low speed of 10^{-6} s^{-1} on an AIMA-5-1 tensile machine in a corrosive environment at cathodic polarization potential. The reference and auxiliary electrodes were used the same as in electrochemical studies. Cathodic polarization potentials –0.750 V, –0.950 V and –1.050 V using PI-50-1.1 potentiostat, were set on the specimen.

2.5. Metallography and Fracture Tests

Microsections for metallographic studies were prepared according to standard technique. To reveal the microstructure, the specimens were etched in a solution of 4% nitric acid in ethyl alcohol. Metallographic studies were performed on a NEOPHOT 21 microscope with an Allied Vision 1800 U-2050c digital camera and SEO ImageLAB software.

The fracture surfaces of the specimens after rupture were examined by scanning electron microscopy with JSM 840 microscope (JEOL, Japan) in the secondary backscattered electron mode at an accelerating voltage of 20 kV and an electron-beam current of 10^{-7}–10^{-10} A.

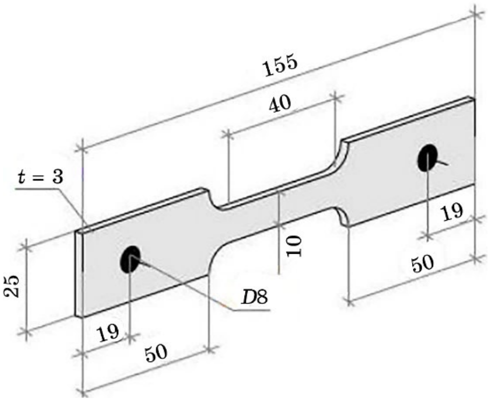

Fig. 2. Sketch of a specimen for slow strain rate tests [36]. The dimensions are provided in millimetres.

2.6. Improvement of the Laboratory Setup for Studying the Susceptibility of Pipe Steels to Stress-Corrosion Cracking under Thin-Film Corrosion Conditions

To take into account the influence of the variable wetting factor, which occurs in the spring–autumn period of the year, a device is developed and manufactured to simulate fluctuations of the solution level in the test cell according to the mode: 50 min in solution and 10 min in air [37].

According to the literature, the highest corrosion rate is observed at a soil moisture level of 20%. Therefore, the laboratory setup for stress-corrosion cracking studying has been improved (Fig. 3): thin-film corrosion was modelled in a soil medium (sand moistened with a solution

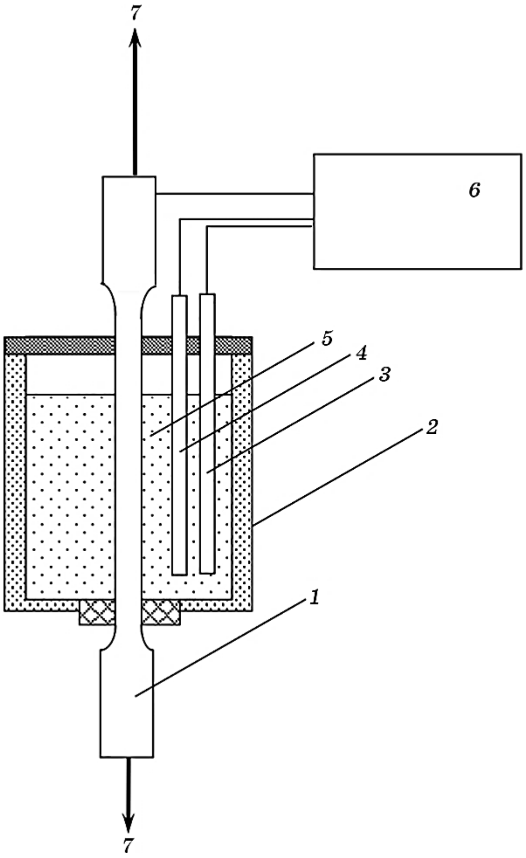

Fig. 3. Experimental setup for studying the susceptibility of pipe steels to stress-corrosion cracking using the slow strain rate tests under conditions simulating thin-film corrosion: *1*—test specimen; *2*—electrochemical cell; *3*—auxiliary electrode; *4*—reference electrode; *5*—model soil environment; *6*—polarization source; *7*—direction of specimen stretching.

to a moisture content of 20%).

3. RESULTS AND DISCUSSION

3.1. Corrosion and Electrochemical Properties of X70 Steel

3.1.1. Study of the Effect of Thin-Film Corrosion on the Corrosion Resistance of X70 Steel

After exposure of the specimens in the solution (Fig. 4, *a*), corrosion products of a dark, almost black colour formed. In the model soil environment (Fig. 4, *b*), the surface was covered with an uneven layer of corrosion products with sand particles firmly attached to the surface. The corrosion rate in the solution was 0.079 mm/year, while in the model soil environment, it almost doubled to 0.146 mm/year (Fig. 4).

Figure 5 shows the change over time in the corrosion potentials of X70 steel in solution and in the model soil environment. Corrosion potential,

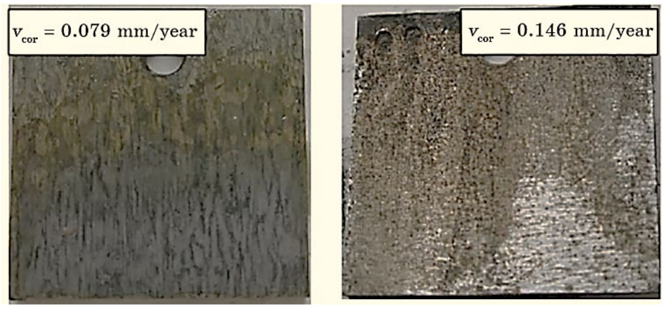

Fig. 4. Appearance of samples after 168 hours of testing at room temperature in solutions: *a*—solution; *2*—model soil environment.

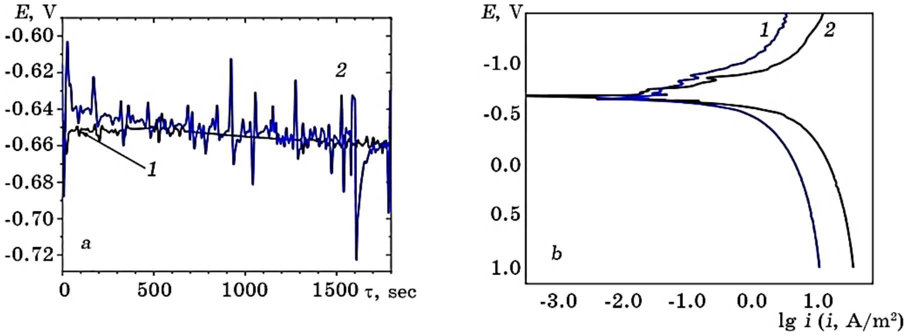

Fig. 5. Corrosion potentials (*a*) and polarization curves (*b*) of X70 steel in solution (*1*) and in the model soil environment (*2*).

TABLE 3. Electrochemical and corrosion properties of X70 steel.

Environment composition	E_{cor}, V	b_a, V	E_{H2}, V	$E^1_{i=0}$, V	$E^2_{i=0}$, V	Mixed mechanism range, V	v_{cor}, mm/year
Solution	−0.649	0.075	−0.864	−0.816	−0.949	0.133	0.079
Model soil environment	−0.656	0.063	−0.907	−1.070	−1.170	0.100	0.146

both in solution and in the soil environment, changes slightly, ranging from –0.652 to –0.649 V and from –0.651 to –0.656 V, respectively (Fig. 5, *a*). It was noted that, in the soil environment, more intense oscillations of the potential were observed compared to the solution. The stable corrosion potential values in both environments differ by 0.007 V, with the corrosion potential being more negative in the model soil environment.

The region of active anodic dissolution in the solution extends from the corrosion potential to –0.09 V, while in the soil environment, it extends to –0.484 V. Their respective lengths are 0.640 V and 0.172 V (Fig. 5, *b*). The slopes of the anodic curves are 0.075 V and 0.063 V (Table 3), confirming the diffusion mechanism of the corrosion process in this solution.

The limiting diffusion current in the solution is almost an order of magnitude higher, than in model soil environment – 0.149 A/m^2 compared to 0.069 A/m^2, indicating the slowing of oxygen delivery to the steel surface in the model soil environment. Hydrogen reduction potential in the solution is lower than in the soil environment, –0.864 V and –0.907 V, respectively, which accelerates its formation at lower cathodic polarization potentials. Since the corrosion rate in the solution is lower than in the model soil environment (0.079 mm/year and 0.146 mm/year), it is assumed that during prolonged contact with the soil environment under limited oxygen access, corrosion mechanism changes, and hydrogen influence activating, which led to increasing in the corrosion rate.

3.1.2. Voltammograms of Fast and Slow Potential Scanning

Figure 6 presents the polarization curves of fast and slow potential scanning for X70 steel. According to the theory proposed by Perkins and developed by Liu [38], the high rate potential scanning polarization curve can be used to assess the electrochemical state of the metal at the crack tip, while the slow rate potential scanning curve is used for crack edges. Typically, null current potential for the slow potential scanning curve is more positive than for the fast scanning curve, indicating to a higher probability of electrochemical reaction occurring at the crack tip compared to areas farther from it due to differences in polarization.

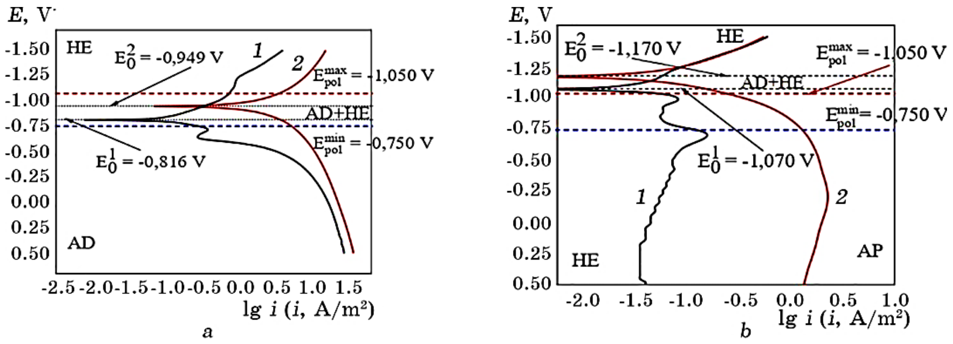

Fig. 6. Potentiodynamic polarization curves of X70 steel in solution (*1*) and in the model soil environment (*2*), obtained at potential scanning rates: *1*—0.5 mV/s; *2*—100 mV/s.

The null current potentials for X70 steel in solution are −0.949 and −0.816 V, respectively (Fig. 6). At potentials more negative than −0.949 V, the cathodic branches of both curves are under cathodic polarization. This indicates that hydrogen evolution occurs both at the crack tip and in the uncracked zone, meaning that stress-corrosion cracking proceeds *via* the hydrogen embrittlement mechanism.

In the potential range from −0.949 to −0.816 V, anodic dissolution occurs at the crack tip, while cathodic hydrogen evolution takes place on the uncracked surface. The hydrogen can diffuse into the metal, accelerating the cracking process. Therefore, in this potential range, stress-corrosion cracking can develop through both the anodic dissolution mechanism and the hydrogen embrittlement mechanism, meaning it follows a mixed mechanism.

In the potential range more positive than −0.816 V, the crack tip and the uncracked area are in the anodic zone, meaning that stress-corrosion cracking proceeds occur by the anodic dissolution mechanism.

In the model environment, the null current potentials are −1.070 and −1.170 V, respectively (Fig. 6, *b*). Thus, in the model environment, in the potential range more positive than −1.070 V, stress-corrosion cracking proceeds *via* the anodic dissolution mechanism, while at potentials negatively than −1.170 V, it follows the hydrogen-embrittlement mechanism.

In the potential range from −1.070 to −1.170 V, stress-corrosion cracking occurs through a mixed mechanism—both anodic dissolution and hydrogen embrittlement. It is worth to note a slight extension of the mixed mechanism region for the soil environment.

Thus, in the model soil environment, a slight narrowing of the mixed mechanism region to 0.100 V was established compared to the width of this region in the solution (0.133 V). Additionally, shifting in the lower boundary of the mixed mechanism potential range to more negative values was noted, reaching –1.070 V (by 0.163 V), while the upper boundary shifted to –1.170 V (by 0.121 V).

These differences in the potential range boundaries indicate variations in the stress-corrosion cracking mechanism. At the minimum protective potential, both in the weakly acidic solution and in the weakly acidic soil environment, stress-corrosion cracking occur *via* the anodic dissolution mechanism. In the solution, hydrogen-embrittlement stress-corrosion cracking occurs at a potential of –0.950 V, which is below the maximum protective potential, whereas in the soil environment, it occurs at potentials more negative than the maximum protective potential. At potentials between –0.950 and –1.050 V in the soil environment, the mixed mechanism of stress-corrosion cracking is realized.

3.2. Slow Strain Rate Tests of X70 Steel

Destruction in air is accompanied by narrowing the specimens near the place of rupture, as a result of which areas, which have undergone plastic deformation, are formed (Fig. 7, curves *1*).

The fracture diagrams of specimens in a solution and in the model soil environment are presented in Fig. 7, and fracture indicators determined during specimens' breaking are shown in Table 4.

It can be considered that the specimen fracture both in air and at a potential of –0.750 V in the solution is mainly ductile, with visible areas of plastic deformation. The fracture line consists of two fragments differing in the direction of fracture (Fig. 8, *a*, *b*).

The relative elongation of specimen after breaking in the solution is 18.52% (Fig. 7, *a*, curve *2*), while the relative reduction in area decreased to 57.54%. The stress-corrosion cracking susceptibility coefficient K_S is of 1.30 (Table 4, Fig. 9).

The fracture line of the specimen breaking at a potential of –0.950 V in solution appears rather stepped, with secondary cracks visible near-

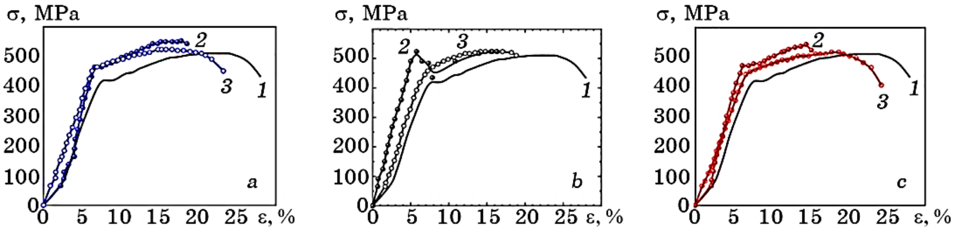

Fig. 7. Fracture curves of X70 steel specimens after mechanical tests in air (*1*), corrosion–mechanical tests in solution (*2*), and in the model soil environment (*3*) at polarization potentials: *a*—–0.750 V; *b*—–0.950 V; *c*—–1.050 V.

TABLE 4. Mechanical properties of X70 steel in air and corrosion–mechanical properties in solution and in a model soil environment at different polarization potentials.

Tests conditions, potential, V	τ_{break}, h	δ, %	S, mm^2	Ψ, %	K_S	Morphology characteristic
Air	43	28.00	7.51	74.95	–	Viscous
Solution 2.28 g/l HCOOH (85%) + 54.4 g/l HCOONa + 10.8 g/l KCNS						
–0.750	32	18.52	12.74	57.54	1.30	Viscous with brittle fragments
–0.950	23	16.31	20.56	31.47	2.38	Predominantly brittle
–1.050	28	15.17	19.97	33.44	2.24	Predominantly brittle
Model soil environment based on 2.28 g/l HCOOH (85%) + 54.4 g/l HCOONa + 10.8 g/l KCNS solution						
–0.750 B	37	23.21	8.78	70.74	1.06	Predominantly brittle
–0.950	31	18.85	13.80	54.01	1.39	Viscous with brittle fragments
–1.050	37	24.29	10.94	63.52	1.18	Viscous with brittle fragments

by, and the plastic deformation area is minimal (Fig. 8, *c*). A reduction in relative elongation to 16.31% (Fig. 7, *b*, curve *2*) and a significant decrease in relative narrowing to 31.47% (Table 4) were noted compared to the fracture characteristics in air, which contributed to an increase in the stress-corrosion cracking susceptibility coefficient K_S to 2.38 (Table 4, Fig. 9).

At the maximum protective potential of –1.050 V, the plastic deformation area of the specimen is practically absent (Fig. 8, *d*). The relative elongation decreased to 15.17% (Fig. 7, *c*, curve *2*), and the relative narrowing to 33.44% (Table 4), which logically led to increasing in the stress corrosion cracking susceptibility coefficient K_S to 2.24 (Table 4, Fig. 9).

In the model soil environment at the minimum protective potential of –0.750 V, as in air, fracture also occurred in a ductile manner and was accompanied by noticeable plastic deformation of the specimen (Fig. 8, *e*). However, the relative elongation was greater than that of the samples in the solution (23.21%) (Fig. 7, *a*, curve *3*). The relative narrowing was also higher than after the fracture of the specimen in the solution, at 70.74% (Table 4). The susceptibility coefficient to stress-corrosion cracking K_S was 1.06 (Table 4, Fig. 9).

After the fracture of specimens in the model soil environment at a potential of –0.950 V, a change in the shape of the fracture line was

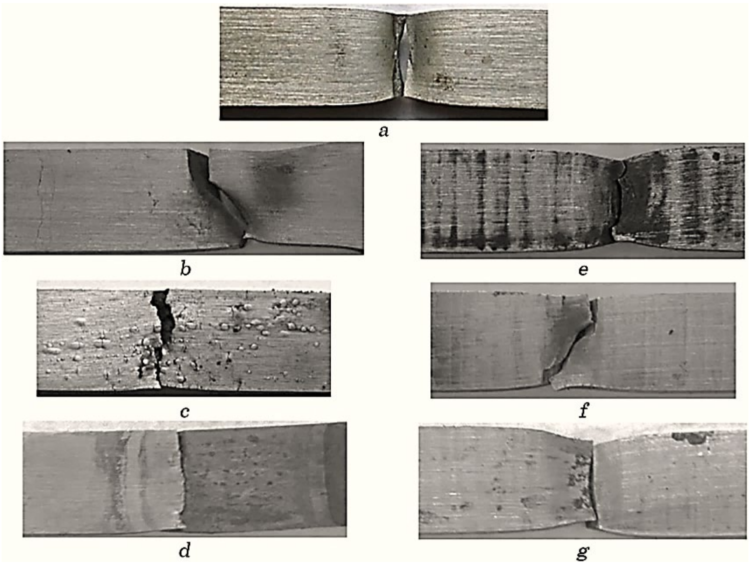

Fig. 8. Appearance of the fracture area of X70 steel specimens after mechanical testing in air (*a*), corrosion–mechanical testing in solution (*b*, *c*, *d*), and in the model soil environment (*e*, *f*, *g*) at cathodic polarization potentials: *a*—–0.750 V; *b*—–0.950 V; *c*—–1.050 V.

observed, with fragments oriented in different directions (Fig. 8, *f*). The relative elongation and narrowing were also greater than these parameters in the solution, at 18.85% (Fig. 7, *b*, curve *3*) and 54.01%, respectively (Table 4). The K_S coefficient was lower than in the solution, nearly at 1.39 (Table 4, Fig. 9).

At the maximum protective potential of –1.050 V, plastic deformation was present but significantly less than in the solution, and the fracture line was relatively smooth (Fig. 8, *g*). The relative elongation was higher than in the solution, at 24.29% (Fig. 7, *c*, curve *3*), while the relative narrowing was 63.52% (Table 4). The susceptibility coefficient to stress-corrosion cracking was 1.18 (Table 4, Fig. 9).

Thus, it has been established that the susceptibility to brittle fracture in the model environment is lower than in the solution. At the minimum protective potential of –0.750 V, differences in the nature of stress-corrosion cracking are relatively small, with K_S being 1.30 in the solution and 1.06 in the model environment (Fig. 9).

Significant changes in the fracture behaviour of X70 steel have been identified at potentials of –0.950 and –1.050 V compared to its fracture in the solution.

In the solution, at potentials of –0.950 V and –1.050 V, stress-corrosion cracking occurs *via* a hydrogen mechanism (Fig. 6, *a*), which satisfactorily correlates with the brittle nature of specimen fracture (Fig.

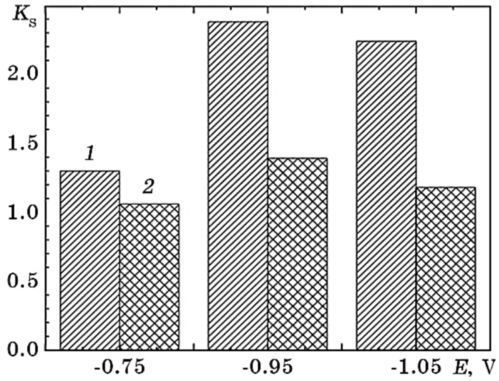

Fig. 9. Change in susceptibility to stress-corrosion cracking of X70 steel specimens after corrosion–mechanical tests in solution (*1*) and model soil environment (*2*), depending on cathodic polarization potentials.

8, *c*, *d*), and K_S values of 2.38 and 2.24, respectively (Table 4). In the model soil environment, at potentials –0.950 and –1.050 V, stress-corrosion cracking occurs *via* the anodic dissolution mechanism (Fig. 6, *b*), which is confirmed by ductile characteristics observed in specimen fracture (Fig. 8, *f*, *g*) and K_S values of 1.39 and 1.18, respectively (Table 4).

3.3. Fractures of Specimens after Slow Stain Rate Tests

Figures 10 and 11 present images of fracture surfaces of X70 steel specimens in air, solution, and in the model soil environment.

Solution. The fracture surface of the specimen tested in air appears fibrous, with distinct signs of plastic shear deformation, formed due to the elongation of large parabolic dimples, including non-metallic inclusions and the rupture of smaller pores (Fig. 10, *a*, a^*), as well as their aggregation. The size of the small dimples corresponds to the grains and subgrains size (up to 4 μm). The appearance of the fracture surface reflects the banded structure of the metal, corresponding to the fracture zone of the pearlitic component, which is oriented along the rolling direction of the steel produced by controlled rolling. This characteristic manifests in larger flat dimples (approximately 20 μm in diameter), which formed due to the plastic shear of pearlite colonies.

In the solution at a test potential of –0.750 V, the fracture surface is more complex than in air, with mixed fracture characteristics observed (Fig. 10, *b*, b^*). Near the specimen surface, a ductile fracture region is formed by shear deformation and the rupture of small pores, with elongated, weakly developed ridges of rupture, but at lower fracture energy compared to air. Further from the edge, part of the fracture, along with the fine dimple rupture, consists of larger quasi-

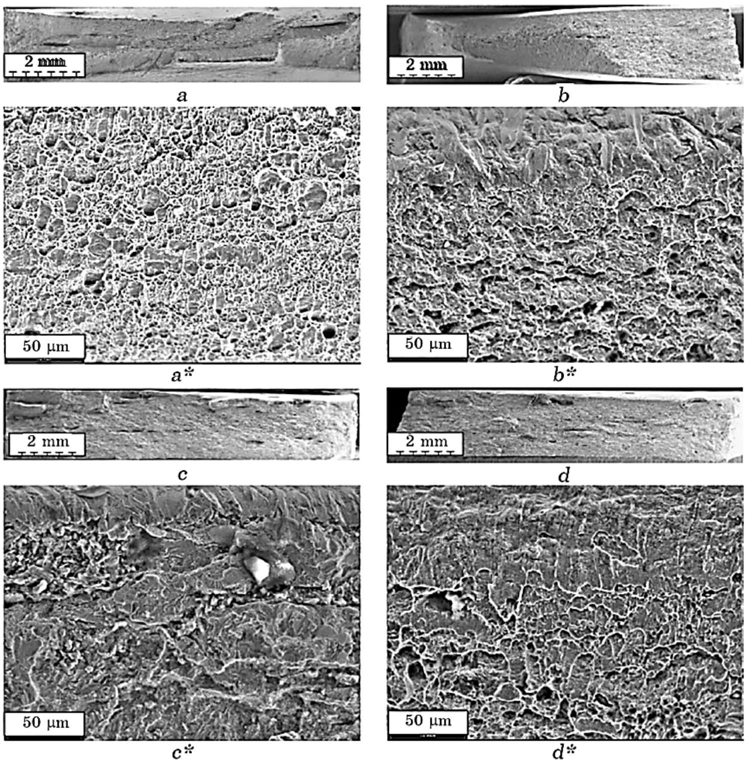

Fig. 10. Fracture surfaces of X70 steel specimens after slow strain rate tests in air (*a*, a^*) and in solution at polarization potentials: *b*, b^*—–0.750 V; *c*, c^*—–0.950 V; *d*, d^*—–1.050 V.

brittle fragments up to 30 μm in size with an almost flat bottom, with remnants of intergranular fracture concentrated primarily in the pearlitic component zone.

At a potential of –0.950 V (Fig. 10, *c*, c^*), fracture details indicate a type of fracture that can be classified as brittle. The entire fracture area consists of large fragments with transverse dimensions ranging from 50 to 90 μm, featuring a textured, fan-shaped bottom and weakly developed rupture ridges along the fragment boundaries. Several loose fracture zones are observed, containing clusters of brittle metal particles and non-metallic inclusions.

At a potential of –1.050 V, a significant portion of the fracture exhibits characteristics of mixed failure (Fig. 10, *d*, d^*). In the larger part of the sample surface adjacent to the edge, fracture occurred through plastic shear deformation. The fracture fragments resemble shear planes and elongated parabolic dimples but with rupture ridges. Another part of the fracture consists of quasi-brittle fragments up to

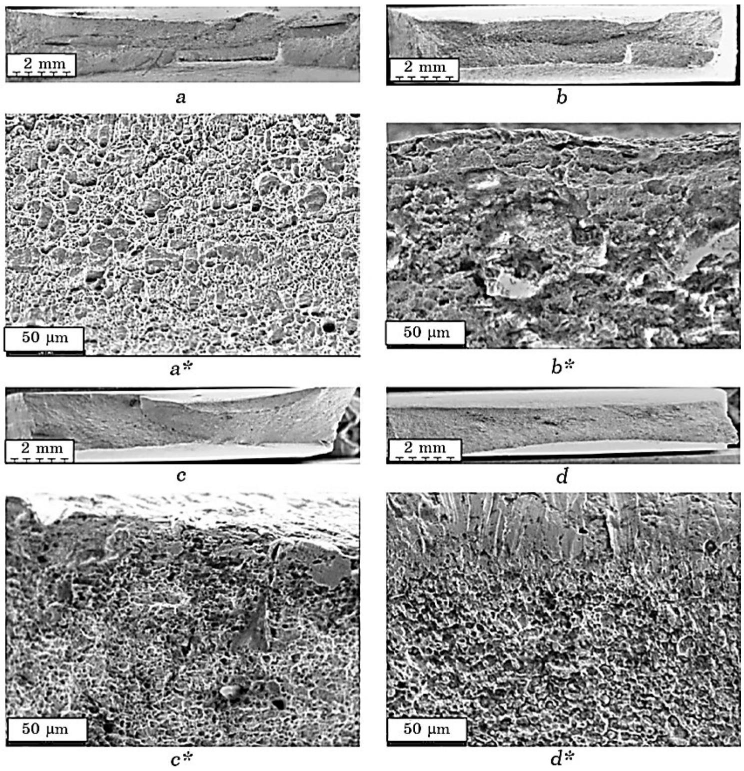

Fig. 11. Fracture surfaces of X70 steel specimens after slow strain rate tests in air (*a*, a^*) and in in the model environment at polarization potentials: *b*, b^*—–0.750 V; *c*, c^*—–0.950 V; *d*, d^*—–1.050 V.

50 μm in size, with an almost flat bottom and remnants of destroyed grains. Cavities are present, which likely formed due to localized hydrogen penetration under the influence of cathodic polarization.

Model Soil Environment. At a potential of –0.750 V, the fracture occurs through a mixed mechanism (Fig. 11, *b*, b^*). The morphology of the fracture surface is predominantly heterogeneous. The part of the specimen near the surface exhibits shear-type fracture characteristics. Further from the specimen edge, at a distance of approximately 0–60 μm from the surface along the fracture plane, a large, irregularly shaped defect is observed, appearing as a deep cavity with a cross-section of approximately 105 μm and a loose surface. This defect was likely formed due to intergranular fracture of fine structural components, caused by internal metal damage due to hydrogen penetration.

The fracture surface of the specimen at a potential of –0.950 V predominantly shows ductile characteristics, but with lower energy expenditures for rupturing small, mostly shallow dimples (Fig. 11, *c*, c^*).

At a distance of 30–50 µm from the sample edge, a region with fracture fragments is identified, appearing as deeper, rounded dark areas ranging from 40 to 75 µm in size with brittle-looking bottoms. These fracture details somewhat resemble the cavity observed in the sample tested at –0.750 V in solution (Fig. 11, *b*, *b**).

The fracture surface of the sample at a potential of –1.050 V exhibits characteristics typical of shear-induced plastic deformation fracture (Fig. 11, *d*, *d**). The remaining surface has a uniform dimpled structure, and ductile fracture occurred through the rupture of small dimples, as well as larger ones formed by the aggregation of shallow but less energy-intensive pores. No typical brittle fragments were observed.

4. CONCLUSIONS

1. Corrosion potential of X70 steel both in a solution of 2.28 g/l HCOOH (85%) + 54.4 g/l HCOONa + 10.8 g/l KCNS and in the soil environment, shows minimal variation, with stable corrosion potential values of –0.649 and –0.656 V, respectively. The active anodic dissolution region in the solution is longer than in the soil-based environment, measuring 0.640 and 0.172 V, respectively. The slopes of the anodic curves are 0.075 and 0.063 V, confirming a diffusion-control corrosion mechanism. Corrosion rates are 0.079 mm/year in solution and 0.146 mm/year in the soil environment. A hypothesis has been proposed regarding a shift in the corrosion mechanism and the activation of hydrogen-induced corrosion during prolonged exposure to the model soil environment with limited oxygen access, which accelerates the steel's corrosion rate.
2. Three potential ranges have been identified where stress-corrosion cracking mechanism of X70 steel varies both in the solution and model soil environment. The boundaries of these ranges and corresponding mechanisms are as follows:

- in solution: for potentials more positive than –0.816 V—anodic dissolution mechanism; for potentials more negative than –0.949 V—hydrogen embrittlement mechanism; from –0.816 to –0.949 V potentials ranger—mixed mechanism;
- in model soil environment: for potentials more positive than –1.070 V – anodic dissolution mechanism, for potentials more negative than –1.170 V—hydrogen embrittlement mechanism, from –1.070 to –1.170 V—mixed mechanism.

A slight narrowing of the mixed mechanism range to 0.100 V in the model soil environment was observed compared to 0.133 V in the solution. Additionally, shifting in the lower limit of the mixed mechanism range to more negative values (–1.070 V) and the upper limit to –1.170 V was noted.

3. It has been established that the susceptibility to brittle fracture at polarization potentials ranging from –0.750 to –1.050 V in the model environment is lower than in the solution. At the minimum protective potential of –0.750 V, differences in the nature of stress-corrosion cracking are minor, with K_S values of 1.30 in the solution and 1.06 in the model environment. Significant changes in the fracture behaviour of X70 steel under thin-film corrosion have been observed at potentials of –0.950 and –1.050 V compared to its fracture in the solution:
- in the solution, stress-corrosion cracking occurs *via* the hydrogen mechanism, which correlates well with the brittle nature of specimen fracture and K_S values of 2.38 and 2.24;
- in the model soil environment, stress-corrosion cracking follows the anodic dissolution mechanism, confirmed by ductile characteristics in specimen fracture and K_S values of 1.39 and 1.18.

ACKNOWLEDGEMENT

This contribution was created under the support of project 'Development of Theoretical and Experimental Bases for Increasing the Resistance to Brittle and Corrosion Cracking of Main Pipelines and Other Structures by Ensuring Appropriate Properties of Welded Joints' by the National Academy of Sciences of Ukraine in 2022–2024 (state registration number 0122U001188).

AUTHORS' CONTRIBUTIONS

L. I. Nyrkova: validation, supervision, funding acquisition, formal analysis, conceptualization, writing review & editing. L. V. Goncharenko: visualization, investigation, formal analysis, writing original draft. S. O. Osadchuk: visualization, methodology, investigation, writing original draft. O. V. Bratochkin: visualization, investigation, data curation, writing original draft.

REFERENCES

1. A. Contreras, M. Salazar, A. Albiter, R. Galván, and O. Vega, *Arc Welding. Publisher InTech*, **16**: 7 (2011).
2. S. A. Abubakar, S. Mori, and J. Sumner, *Metals*, **12**, No. 8: 1397 (2022).
3. I. S. Cole and D. J. C. S. Marney, *Cor. Sci.*, **56**: 5 (2012).
4. K. Yin, H. Liu, and Y. F. Cheng, *Cor. Sci.*, **145**: 271 (2018).
5. M. Wasim and M. B. Djukic, *J. Nat. Gas Sci. Eng.*, **100**: 104467 (2022).
6. M. Wasim, S. Shoaib, N. M. Mubarak, Inamuddin, and A. M. Asiri, *Environ. Chem. Lett.*, **16**: 861 (2018).
7. S. Suganya and R. Jeyalakshmi, *J. Mater. Eng. Perform.*, **28**: 863 (2019).
8. H. M. Ezuber, A. Alshater, S. Z. Hossain, and A. El-Basir, *Arab. J. Sci. Eng.*,

46: 6177 (2021).
9. A. A. Oskuie, T. Shahrabi, A. Shahriari, and E. Saebnoori, *Cor. Sci.*, **61**: 111 (2012).
10. S. Bordbar, M. Alizadeh, and S. H. Hashemi, *Mater. Des.*, **45**: 597 (2013).
11. P. Liang, X. Li, C. Du, and X. Chen, *Mater. Des.*, **30**, No. 5: 1712 (2009).
12. L. Y. Xu and Y. F. Cheng, *Cor. Sci.*, **59**: 103 (2012).
13. B. T. Lu, F. Song, M. Gao, and M. Elboujdaini, *Cor. Sci.*, **52**, No. 12: 4064 (2010).
14. A. Eslami, R. Kania, B. Worthingham, G. V. Boven, R. Eadie, and W. Chen, *Cor. Sci.*, **53**, No. 6: 2318 (2011).
15. B. T. Lu, J. L. Luo, P. R. Norton, and H. Y. Ma, *Acta Mater.*, **57**, No. 1: 41 (2009).
16. R. N. Parkins, W. K. Blanchard, and B. S. Delanty, *Corrosion*, **50**, No. 05: 394 (1994).
17. I. M. Gadala and A. Alfantazi, *Cor. Sci.*, **82**: 45 (2014).
18. Z. Y. Liu, X. Z. Wang, C. W. Du, J. K. Li, and X. G. Li, *Mat. Sci. Eng.: A*, **658**: 348 (2016).
19. Y. Murakami, T. Kanezaki, and Y. Mine, *Metall. Mater. Trans. A*, **41**: 2548 (2010).
20. R. Miresmaeili, L. Liu, and H. Kanayama, *Int. J. Press. Vessel. Pip.*, **99**: 34 (2012).
21. X. C. Ren, W. Y. Chu, Y. J. Su, J. X. Li, L. J. Qiao, B. Jiang, and G. Chen, *Mat. Sci. Eng.: A*, **491**: 164 (2008).
22. S. Wu, Z. Gao, Y. Liu, and W. Hu, *Cor. Sci.*, **218**: 111184 (2023).
23. Z. Y. Liu, Q. Li, Z. Y. Cui, W. Wu, Z. Li, C. W. Du, and X. G. Li, *Constr. Build. Mater.*, **148**: 131 (2017).
24. K. Gong, M. Wu, F. Xie, G. Liu, and D. Sun, *Constr. Build. Mater.*, **260**: 120478 (2020).
25. Z. Y. Liu, X. G. Li, Y. Zhang, C. W. Du, and G. Zhai, *Acta Metall. Sin. (English Letters)*, **22**: 58 (2009).
26. Z. Y. Liu, X. G. Li, C. W. Du, G. L. Zhai, and Y. F. Cheng, *Cor. Sci.*, **50**: 2251 (2008).
27. Z. Y. Liu, X. G. Li, C. W. Du, L. Lu, Y. R. Zhang, and Y. F. Cheng, *Cor. Sci.*, **51**, Iss. 4: 895 (2009).
28. X. Chen, C. W. Du, X. G. Li, C. He, P. Liang, and L. Lu, *Int. J. Miner. Metall. Mater.*, **16**, Iss. 5: 525 (2009).
29. X. Li, J. Liu, J. Sun, X. Lin, C. Li, and N. Cao, *Cor. Sci.*, **160**, P. 2: 108167 (2019).
30. Z. Liu, C. Du, X. Zhang, F. Wang, and X. Li, *Acta Metall. Sin. (English Letters)*, **26**: 489 (2013).
31. Z. Y. Liu, X. G. Li, C. W. Du, and Y. F. Cheng, *Cor. Sci.*, **51**, Iss. 12: 2863 (2009).
32. D. Wang, F. Xie, M. Wu, G. Liu, Y, Zong, and X. Li, *Metall. Mater. Trans. A*, **48**: 2999 (2017).
33. X. Li, J. Liu, J. Sun, X. Lin, C. Li, and N. Cao, *Cor. Sci.*, **160**: 108167 (2019).
34. Z. Liu, G. Zhai, X. Li, and C. Du, *J. Miner. Metall. Mater.*, **15**, Iss. 6: 707 (2008).
35. *ISO 3183:2019 Petroleum and Natural Gas Industries – Steel Pipe for Pipeline Transportation Systems*.
36. L. Nyrkova, L. Goncharenko, S. Osadchuk, O. Bratochkin, and S. Kovalenko, *Proc. of Conference 'Mechanical Technologies and Structural Materials' (September 20–24, 2024, Split, Croatia)*, **2024**: 317 (2024).
37. L. I. Nyrkova, A. O. Rybakov, S. O. Osadchuk, S. L. Melnychuk, N. O. Gapula, and H. M. Yakovenko, *Ukrainian Patent*, 107229: 1 (2014).
38. Z. Y. Liu, X. G. Li, and Y. F. Cheng, *Electrochem. Commun.*, **12**, Iss. 7: 936 (2010).